

The Scalable Analytical Model for Calculating the Magnetic Field of Surface-Mounted Permanent Magnet Motor

Zhaokai Li , *Member, IEEE*, Xiaoyan Huang , *Member, IEEE*, and Luca Peretti , *Senior Member, IEEE*

Abstract—This article develops a scalable analytical model that builds a relationship between any surface-mounted permanent magnet (SPM) motor and a general motor with variable slot-opening and air-gap length, considering both the saturation effect and slotting effect. It can not only give the performance of the single SPM motor but also show internal connection among different SPM motors regardless of the motor power and dimension. To account for the iron saturation, the equivalent saturation current combined with simplified BH curves of iron is introduced to directly present the iron magnetic potential distribution without an iterative process. Thus, the proposed model can be used as the surrogate model in the motor design with little computation and provide great insight into the relationship among motors with different power and dimension. Both finite-element analysis and experiment are carried out to validate the proposed model.

Index Terms—Analytical model, scaling law, surface-mounted permanent magnet (SPM) motor.

I. INTRODUCTION

THE permanent magnet (PM) motor plays a critical role in advancing transportation electrification and has received enormous attention in road vehicles, boats, and airplanes due to their high efficiency and torque density. Driven by the increasing demand for energy-efficient and environmentally friendly technology, the optimization and design of high-performance PM motors have become significant in the process of transportation electrification [1], [2], [3], [4], [5].

In the recent development of motor design, researchers focus on two aspects, i.e., building a computationally efficient surrogate model and developing an excellent optimization algorithm.

Manuscript received 21 April 2023; revised 15 September 2023 and 5 December 2023; accepted 31 January 2024. This work was supported by the "STandUP for Energy". (Corresponding authors: Xiaoyan Huang; Luca Peretti.)

Zhaokai Li and Luca Peretti are with the Division of Electric Power and Energy Systems, KTH Royal Institute of Technology, 11428 Stockholm, Sweden (e-mail: zhaokai@kth.se; lucap@kth.se).

Xiaoyan Huang is with the Zhejiang Provincial Key Laboratory of Electrical Machine Systems, College of Electrical Engineering, Zhejiang University, Hangzhou 310027, China (e-mail: xiaoyanhuang@zju.edu.cn).

Color versions of one or more figures in this article are available at <https://doi.org/10.1109/TIE.2024.3363770>.

Digital Object Identifier 10.1109/TIE.2024.3363770

The former tries to obtain the relationship between the objectives and the inputs for the motor geometry, while the latter requires finding the global optimal solution with minimum calculation. This article focuses on the surrogate model with high computational efficiency and physical insight [6].

The finite element method (FEM) is the most accurate surrogate model to calculate motor performance and therefore it is widely used for the optimization of motors [7], [8], [9]. However, it is time-consuming. The space-mapping technique employs the coarse model to align with a fine model for reducing the computation burden [10], [11], [12]. However, the accuracy of the coarse model is greatly affected by the quality of evaluation in the fine model, which still requires significant computation.

Similarly, a scalable saturated model for PM motors was proposed in [13] and [14] to accurately and efficiently calculate the motor efficiency map, but there was a lack of theoretical explanation for the assumption of the dimensional scaling between small-scale and large-scale PM motors. This article will focus on the scaling equivalence of different surface-mounted permanent magnet (SPM) motors.

The analytical models can be good candidates as surrogate models [15]. When accounting for the slotting effect in the more conventional SPM motor, the subdomain technique was proposed in calculating the air-gap flux density [16], ac copper loss [17], and magnet loss [18] of SPM motors. It is also suitable for interior PM motors [19], vernier PM motors [20], and spoke-type PM motors [21].

The conformal mapping technique is another way to calculate the slotted air-gap flux density combined with the general solution of the slotless air-gap flux density for the PM motor [22], [23], [24]. It shows the mathematical and theoretical relationship between the motor performance and motor parameters for the surrogate model. However, the matrix inversion in the subdomain models and the Schwarz-Christoffel (SC) transformation in the conformal mapping models make such a relationship indirect and unclear. Meanwhile, the magnetic circuit model has been widely used to predict motor performance [25], [26], [27]. Recently, more and more research has focused on the combination of the linear analytical model and magnetic circuit model to improve accuracy, but they all require iterative calculation to determine the saturation level [28], [29].

This article develops a scalable analytical model (SAM) for calculating the magnetic field of SPM motors considering

both the saturation effect and slotting effect. The details of the conformal mapping for the general motor are preserved as a database with variable slot-opening and air-gap length. Then, the new SPM motors with either an outer rotor or an inner rotor configuration are mathematically transformed into the general motor and the SC mapping for the new SPM motors can be extracted from the database of the general motor to significantly reduce the calculation time while considering slotting effect. Then, the equivalent saturation current is introduced to consider the saturation effect according to the equivalence between current and magnetic potential drop of iron. No iteration calculation is required to obtain the equivalent saturation current when using simplified BH curves of iron. The proposed model can predict both large-scale and small-scale SPM motors with either an outer rotor or an inner rotor configuration, showing the internal relationship among all the motors with different power and dimension. A FEM of a small-power and a large-power motor is carried out to verify the effectiveness of the proposed model, while the experimental results of a small-power motor prototype show great accuracy. The proposed model not only gives physical insight into the relationship among different motors regardless of the motor power and dimension but also helps to improve the calculation efficiency for the initial optimization or as the surrogate model.

II. SCALABLE ANALYTICAL MODEL

The SAM uses the following assumptions.

- 1) The relative permeability of the magnet is 1.
- 2) The end effect and eddy current effect are neglected.
- 3) The influence of iron saturation is neglected.

A. General Motor Model

The general motor is introduced as the benchmark of all the SPM motors. The air-gap radius near the stator bore R_s and the tooth length h_t are both equal to 1 m. It has three open slots ($Q_0 = 3$), as the slot numbers of all three phase PM motors are multiples of 3. Therefore, it is convenient to make a scalable transformation between the new motor and the general motor in terms of the angle variation of slot shape. Besides, a small slot number helps save the computational resources for building the database of the general motor. The slot-opening angle b_{so} and total air-gap length l_a varies from 20° to 100° at the step of 1° and from 0.1 to 0.9 m at the step of 0.01 m, respectively. It is noted that the total air-gap length includes the length of the air-gap and magnet. The schematic view of the general motor is given in Fig. 1(a).

The air-gap field solution of the general motor is investigated using the conformal mapping technique. There are three conformal mappings to transform the constantly permeable region of air-gap, magnet, and slot into an annulus, as shown in Fig. 1(b)–(d) [24]

$$T_g = e^{Z_g} \quad (1)$$

$$Z_g = Z_0 + Z_1 \int_{w_0}^w \prod_{k=1}^{n-1} (W_g - w_k)^{\alpha_k - 1} dW_g \quad (2)$$

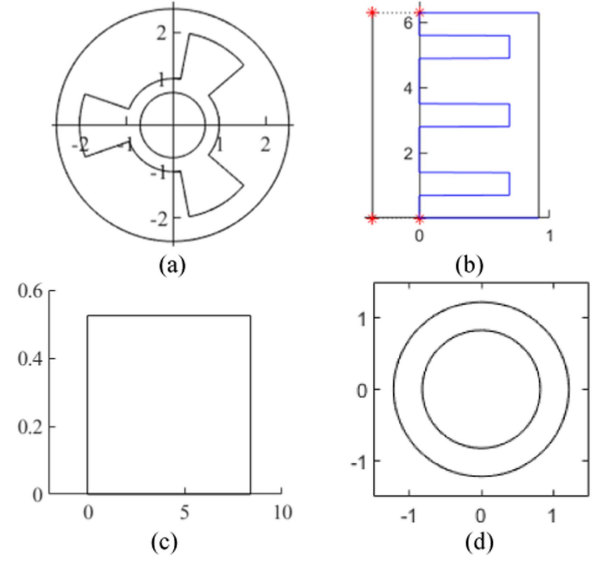


Fig. 1. Conformal mapping of the general motor. (a) T_g plane. (b) Z_g plane. (c) W_g plane. (d) φ_g plane.

$$\varphi_g = e^{-j[\frac{2}{\Delta x}(W_g - j\frac{\Delta y}{2}) - 1]\pi} \quad (3)$$

where SC mapping is expressed using (2) [31]. Z_0 , Z_1 , w_k , and α_k are the SC parameters in (2). As numerical calculation is always required to obtain these parameters and employ SC mapping, it is feasible to replace this time-consuming process with the database of SC mapping based on the general motor. Even though the database setup based on the general motor takes much effort, it is worthwhile because it is applicable to all SPM motors with either an outer rotor or an inner rotor configuration.

Meanwhile, both winding current and PMs should be transformed into the equivalent dot current in the constant-permeability region of the general motor. The winding current is located at the center of each slot, i.e., $(r_{w\varphi}, \theta_{w\varphi})$. The value of winding current \mathbf{I}_w is calculated using

$$\mathbf{I}_w = \mathbf{M}_s [i_a \ i_b \ i_c]^T \quad (4)$$

where i_a , i_b , and i_c are the instantaneous phase currents, and \mathbf{M}_s is the constant matrix derived from the winding layout.

The nonlinear BH curves of PMs are usually employed to check the demagnetization risk of PM motors [32]. Under normal conditions, the flux density in PMs is above the knee point to avoid demagnetization. Therefore, the linear relationship between flux density and magnetic field strength in PMs is employed to replace the nonlinear BH curves of PMs in the analytical model. The equivalent magnet current is placed along both sides of the PMs. The PM position is represented using $(r_{PM\varphi}, \theta_{PM\varphi})$, while the value of the equivalent magnet current \mathbf{I}_M is calculated using [33]

$$\mathbf{I}_M = \frac{B_r h_m}{\mu_0 N_m} \mathbf{M}_m \quad (5)$$

where B_r , h_m , and N_m are the magnet remanence, magnet thickness, and the number of equivalent magnet current. \mathbf{M}_m is a constant matrix derived from the pole number, consisting of -1 and

1 to show the polarity of the magnet. Then, the vector magnetic potential $A_k(r_\varphi, \theta_\varphi, r_{k\varphi}, \theta_{k\varphi})$ in the constant-permeability region of the general motor produced by the equivalent dot current $i_k(r_{k\varphi}, \theta_{k\varphi})$ can be calculated in annulus region, as the conformal mapping keeps the scalar magnetic potential unchanged. It is noted that i_k represents the values of winding current \mathbf{I}_w and equivalent magnet current \mathbf{I}_M while the position $(r_{k\varphi}, \theta_{k\varphi})$ includes the winding current positions $(r_{w\varphi}, \theta_{w\varphi})$ and the PM positions $(r_{PM\varphi}, \theta_{PM\varphi})$. Hence, the general solution of $A_k(r_\varphi, \theta_\varphi, r_{k\varphi}, \theta_{k\varphi})$ is expressed as [24], [30]

$$A_k = \frac{\mu_0 i_k}{2\pi} \left\{ \ln \left(\sqrt{r_\varphi^2 + r_{k\varphi}^2 - 2r_\varphi r_{k\varphi} \cos(\theta_\varphi - \theta_{k\varphi})} \right) - \sum_{k=1}^{+\infty} \frac{r_\varphi^k r_{s\varphi}^{-k} \left(r_{k\varphi}^{2k} + r_{r\varphi}^{2k} \right) + r_\varphi^{-k} r_{r\varphi}^{2k} \left(r_{s\varphi}^{-2k} r_{k\varphi}^{2k} + r_{s\varphi}^k \right)}{k \left(r_{s\varphi}^{2k} - r_{r\varphi}^{2k} \right)} \cos(k(\theta_\varphi - \theta_{k\varphi})) \right\} \quad (6)$$

where $(r_\varphi, \theta_\varphi)$ represents the position of the vector magnetic potential A_k . $r_{s\varphi}$ and $r_{r\varphi}$ are the inner and outer radius of the annulus in Fig. 1(d).

The total vector magnetic potential can be obtained based on the principle of superposition. It can be seen that the variation of the magnetic field in the SPM motor results from the change of the winding current value \mathbf{I}_w and the PM positions $(r_{PM\varphi}, \theta_{PM\varphi})$. Therefore, the total radial and tangential air-gap flux density $B_r(r, \theta)$ and $B_\theta(r, \theta)$ in the slotted air-gap of the T_g plane can be calculated as [24], [30]

$$\begin{aligned} \vec{B} &= B_r + jB_\theta = \lambda^* \sum_{k=1}^{N_k} (B_{r\varphi k} + jB_{\theta\varphi k}) \\ &= -\mu_0 \left(\frac{\partial \varphi_g}{\partial W_g} \frac{\partial W_g}{\partial Z_g} \frac{\partial Z_g}{\partial T_g} \right)^* \sum_{k=1}^{N_k} \left(\frac{\partial \varphi_k}{\partial r_\varphi} + j \frac{1}{r} \frac{\partial \varphi_k}{\partial \theta_\varphi} \right) \quad (7) \end{aligned}$$

where $B_{r\varphi k}$ and $B_{\theta\varphi k}$ are the radial and tangential air-gap flux density in the annulus of the φ_g plane. λ is the complex permeance function from the conformal mapping using (1)–(3). N_k is the number of the total current, including \mathbf{I}_w and \mathbf{I}_M . In (7), only the item $\frac{\partial W_g}{\partial Z_g}$ requires an iterative calculation for solving the SC mapping using (2). This term will be replaced by the database of SC mapping at different slot-opening angles and air-gap lengths for this general motor. Any other SPM motor will be converted to the general motor for calculating the new magnetic field based on the database of SC mapping. Therefore, a clear relationship between the motor performance and motor dimension can be revealed using the explicit formula and the constant database.

In Fig. 1(a), the slot shape of the general motor is simplified using the open-slot type. To investigate the influence of shape, slot depth and slot angle in semi-closed slots, the complex permeance function λ is presented to show their relationship in Fig. 2. When the slot-opening angle $b_{so} = 40^\circ$, total air-gap length $l_a = 0.3$ m, and the tooth-tip height $h_{tip} = 0.2$ m, different slot depths (0.001, 1, and 10 m) and different slot angles (45° , 80° , and 115°) are chosen to calculate the complex permeance function. Fig. 2 shows that they have a negligible influence on λ .

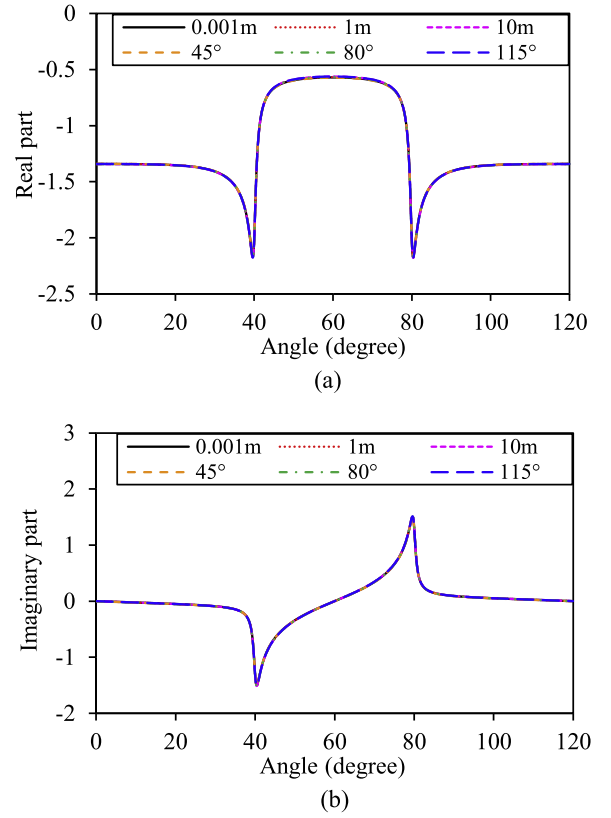


Fig. 2. Complex permeance function at different slot angles and air-gap lengths. (a) Real part of λ . (b) Imaginary part of λ .

A similar simplification has also been used in [23]. Therefore, the database of SC mapping is established only with the variation of slot angle and air-gap length.

B. Scalable Transformation Principle

The slot number q and air-gap radius r_s in the new SPM motor are the key parameters to transform the motor dimension into that of the general motor. The transformation process for both outer rotor and inner rotor SPM motors into the general motor is given in Fig. 3. It consists of two steps. In Step 1, the original slotted air-gap is converted into the polygon using the logarithmic function. In the next step, only one-slot constant-permeability region is selected to make this transformation simple and fast while keeping the same accuracy, which is displayed in the red dashed rectangle for Z plane in Fig. 3. Step 2 presents the linear conformal mapping to uniformly scale and move the air-gap polygon in Z plane to Z_g plane. Thus, these two steps merge into the following conformal mapping function:

$$T = e^Z = e^{k_q [Z_g - \ln(R_s)] + \ln(r_s)} \quad (8)$$

for inner rotor SPM motors and

$$T = e^Z = e^{-k_q [Z_g - \ln(R_s) - 2\pi j] + \ln(r_s)} \quad (9)$$

for outer rotor SPM motors, where $k_q = Q_0/q = 3/q$.

Then, according to the database of SC parameters for the general motor, the single-slot region in the Z_g plane can be

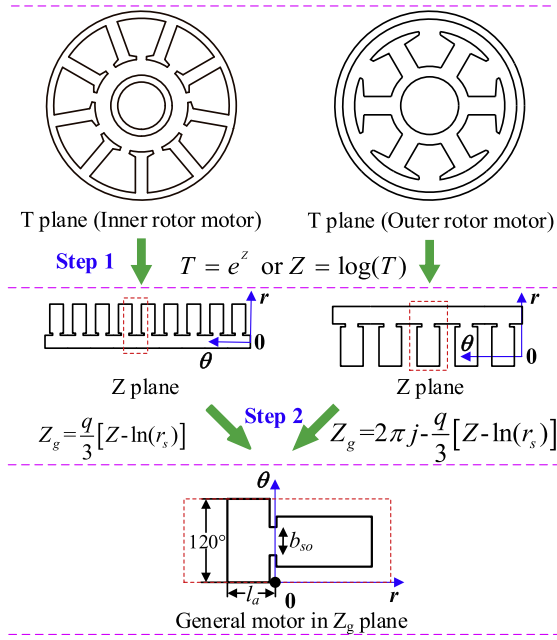


Fig. 3. Transformation between the new motor and the general motor.

conformally mapped to the rectangular region in the W_g plane, as shown in Fig. 1(b)–(c). Considering the different slot numbers between the new motor and the general motor, the new conformal mapping between W_g plane and φ_g plane is manipulated from (3)

$$\varphi_g = e^{-j \left[\frac{2}{k_q \Delta x} (W_g - j \frac{\Delta y}{2}) - 1 \right] \pi}. \quad (10)$$

The parameter k_q represents the influence of the slot number on the air-gap field of the SPM motor. Therefore, the positions of scalar magnetic potential (r, θ) and the equivalent current $(r_{k\varphi}, \theta_{k\varphi})$ are transformed to that of $(r_\varphi, \theta_\varphi)$ and $(r_{k\varphi}, \theta_{k\varphi})$ in the annulus of φ_g plane for the new SPM motor using (8)–(10). The analytical solution of $A_k(r_\varphi, \theta_\varphi, r_{k\varphi}, \theta_{k\varphi})$ in (6) can be calculated accordingly. To make the SAM compatible with both outer rotor and inner rotor SPM motors, the analytical solution of air-gap flux density in the φ_g plane should be expressed in the Cartesian coordinate

$$\begin{aligned} \vec{B}_\varphi &= B_{x\varphi} + jB_{y\varphi} \\ &= -\mu_0 \sum_{k=1}^{N_k} \left(\frac{\partial A_k}{\partial r_\varphi} \cos(\theta_\varphi) - \frac{1}{r} \frac{\partial A_k}{\partial \theta_\varphi} \sin(\theta_\varphi) \right) \\ &\quad + j \left(\frac{\partial A_k}{\partial r_\varphi} \sin(\theta_\varphi) + \frac{1}{r} \frac{\partial A_k}{\partial \theta_\varphi} \cos(\theta_\varphi) \right). \end{aligned} \quad (11)$$

The complex permeance function can be expressed as the explicit expression

$$\lambda = \pm \frac{2\pi j \mu_0 r_\varphi}{\Delta x k_q r Z'_g} e^{j(\theta_\varphi - \theta)} \quad (12)$$

where $(Z_g)'$ is the derivative of the SC transformation using (2), which is also included in the database for the general motor. The sign “+” and “−” are for the inner rotor and outer rotor

SPM motors, respectively. Therefore, the air-gap flux density at the position (r, θ) in the T plane is derived from (7)

$$\begin{aligned} \vec{B} &= B_x + jB_y = (\lambda_a - j\lambda_b) (B_{x\varphi} + jB_{y\varphi}) \\ &= B_r + jB_\theta = (\lambda_a B_{x\varphi} + \lambda_b B_{y\varphi}) \cos(\theta) \\ &\quad + (\lambda_a B_{y\varphi} - \lambda_b B_{x\varphi}) \sin(\theta) \\ &\quad + j(\lambda_a B_{y\varphi} - \lambda_b B_{x\varphi}) \cos(\theta) \\ &\quad - j(\lambda_a B_{x\varphi} + \lambda_b B_{y\varphi}) \sin(\theta). \end{aligned} \quad (13)$$

The expression of the flux φ_{ti} flowing into every tooth is simplified as

$$\varphi_{ti}(t) = R_s l_{\text{eff}} [A_k(\theta_{ti2}) - A_k(\theta_{ti1})] \quad (14)$$

where l_{eff} is the effective length of the SPM motor in the axial direction. θ_{ti1} and θ_{ti2} are the angles of the slot center for the i th tooth. The flux linkage $\psi_{\text{ABC}}^{\text{all}}$ of each phase is calculated from the total flux flowing into the tooth based on the winding layout and the back-EMF is expressed as

$$U_{\text{ABC}} = -\frac{d\psi_{\text{ABC}}}{dt}. \quad (15)$$

The inductance of the motor L_{ABC} is calculated as

$$L_{\text{ABC}} = \psi_{\text{ABC-w}} \mathbf{I}_{\text{ABC}}^{-1} \quad (16)$$

where the flux linkage $\psi_{\text{ABC-w}}$ is produced by the phase winding current \mathbf{I}_{ABC} and it can be obtained using (14).

According to the Maxwell stress tensor, the electromagnetic torque is calculated as

$$T = \frac{l_{\text{eff}} r^2}{\mu_0} \int_0^{2\pi} B_r(r, \theta) B_\theta(r, \theta) d\theta. \quad (17)$$

The electromagnetic force in the Cartesian coordinate is obtained using the Maxwell stress tensor [34]

$$\begin{aligned} F_x &= \frac{r l_{\text{eff}}}{2\mu_0} \int_0^{2\pi} [(B_\theta^2 - B_r^2) \cos(\theta) + 2B_r B_\theta \sin(\theta)] d\theta \\ F_y &= \frac{r l_{\text{eff}}}{2\mu_0} \int_0^{2\pi} [(B_\theta^2 - B_r^2) \sin(\theta) - 2B_r B_\theta \cos(\theta)] d\theta. \end{aligned} \quad (18)$$

As for the electromagnetic loss prediction, different loss models can be used to predict the motor loss based on the analytical solution of magnetic field distribution in the SPM motor. In the PMs, the eddy current and the corresponding loss are calculated using [29]

$$J_{\text{eddy}}(t) = -\sigma \sum_{k=1}^{N_k} \frac{\partial A_k}{\partial t} + C_{p0}(t) \quad (19)$$

$$P_{\text{eddy}} = \frac{l_{\text{eff}}}{\sigma} \iint_S J_{\text{eddy}}^2(t) dS \quad (20)$$

where σ is the conductivity of the material. S is the area of the PM region. $C_{p0}(t)$ is introduced to guarantee that the total eddy current in the single conductor equals zero in the PM region. It

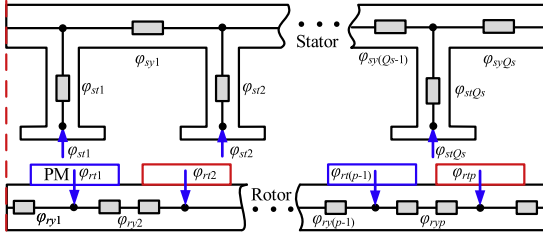


Fig. 4. Flux distribution in the stator iron.

is expressed as [29]

$$C_{p0}(t) = \frac{\sigma}{S} \sum_{k=1}^{N_k} \iint_S \frac{\partial A_k}{\partial t} dS. \quad (21)$$

For the iron loss in the stator and rotor, the Steinmetz equation is used to estimate the value. According to Bertotti's theory, the total iron loss is calculated as [35]

$$\begin{aligned} P_{\text{iron}} &= P_{\text{hys}} + P_c + P_e \\ &= k_h f B_m^\beta + k_c (f B_m)^2 + k_e (f B_m)^{1.5} \end{aligned} \quad (22)$$

where the coefficients k_h , k_c , k_e , and the parameter β are extracted from the experiment at the peak magnetic flux density B_m and frequency f . Based on the harmonic analysis theory, the waveform of iron flux density can be decomposed into a series of harmonic components. The iron loss is the sum of the losses originating from the fundamental and harmonic field using (22) [36].

For the copper loss, the phase resistance of the motor can be derived from Ohm's law when neglecting the eddy current effect [37]

$$R_{\text{copper}} = \frac{k_{\text{end}} \rho q N_c^2 l_{\text{eff}}}{12 k_s S_{\text{slot}}} \quad (23)$$

where q is the slot number. N_c is the number of conductors per slot. k_s is the slot fill factor and S_{slot} is the area of one slot. k_{end} represents the extra resistance due to the end winding ($k_{\text{end}} > 1$). The corresponding copper loss can be calculated using

$$P_{\text{copper}} = 3 I_m^2 R_{\text{copper}}. \quad (24)$$

Finally, the electromechanical conversion efficiency from the electric power input to the mechanical power output can be predicted using the following equation:

$$\eta = \frac{\frac{2\pi T_n}{60}}{\frac{2\pi T_n}{60} + P_{\text{iron}} + P_{\text{eddy}} + P_{\text{copper}}} \quad (25)$$

when the windage loss and friction loss are neglected.

C. Flux Density of Stator and Rotor

The flux density in the stator and rotor is the key parameter to decide whether the local iron saturation should be included in the SAM. Therefore, a simple magnetic circuit is used to predict the iron flux density without considering the iron saturation, as shown in Fig. 4.

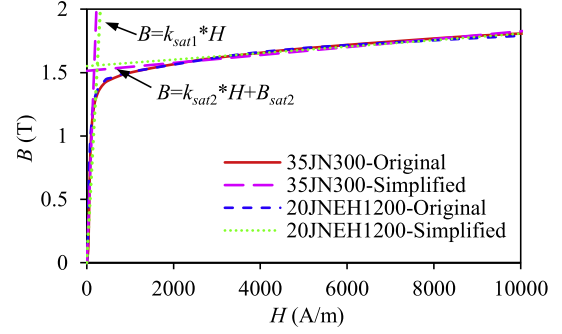


Fig. 5. BH curves of the electrical steel for SPM motors.

According to Kirchhoff's circuit laws, the stator tooth flux φ_{ti} , the stator yoke flux φ_{syi} , and the rotor flux φ_{ryi} are calculated as

$$\begin{bmatrix} -1 & 1 & 0 & \cdots & 0 & 0 \\ 0 & -1 & 1 & \cdots & 0 & 0 \\ \vdots & \vdots & \vdots & \ddots & \vdots & \vdots \\ 0 & 0 & 0 & \cdots & -1 & 1 \end{bmatrix} \begin{bmatrix} \varphi_{sy1} \\ \varphi_{sy2} \\ \vdots \\ \varphi_{syQ_s} \end{bmatrix} = \begin{bmatrix} \varphi_{st2} \\ \varphi_{st3} \\ \vdots \\ \varphi_{stQ_s} \end{bmatrix} \quad (26)$$

$$\begin{bmatrix} -1 & 1 & 0 & \cdots & 0 & 0 \\ 0 & -1 & 1 & \cdots & 0 & 0 \\ \vdots & \vdots & \vdots & \ddots & \vdots & \vdots \\ 0 & 0 & 0 & \cdots & -1 & 1 \end{bmatrix} \begin{bmatrix} \varphi_{ry1} \\ \varphi_{ry2} \\ \vdots \\ \varphi_{ryp} \end{bmatrix} = \begin{bmatrix} \varphi_{rt2} \\ \varphi_{rt3} \\ \vdots \\ \varphi_{rtp} \end{bmatrix} \quad (27)$$

when neglecting the slot leakage. Q_s and p are the slot and pole number of the motor. Besides, the magnetic potential of stator yoke and rotor yoke is used to solve (26) and (27) using Ohm's law

$$\begin{aligned} \frac{l_{sy}}{k_{sat1} S_{sy}} \varphi_{sy1} + \frac{l_{sy}}{k_{sat1} S_{sy}} \varphi_{sy2} + \cdots + \frac{l_{sy}}{k_{sat1} S_{sy}} \varphi_{syQ_s} &= 0 \\ \frac{l_{ry}}{k_{sat1} S_{ry}} \varphi_{ry1} + \frac{l_{ry}}{k_{sat1} S_{ry}} \varphi_{ry2} + \cdots + \frac{l_{ry}}{k_{sat1} S_{ry}} \varphi_{ryp} &= 0 \end{aligned} \quad (28)$$

where k_{sat1} is the slope of the simplified BH curve in the unsaturated region of Fig. 5. l_{sy} , S_{sy} , l_{ry} , and S_{ry} are the length and the cross-sectional area of the magnetic resistance in the stator yoke and rotor yoke, respectively.

The matrix form of (26)–(28) is expressed as

$$\Phi_{\text{iron}} = \mathbf{A}_{\text{iron}} \Phi_{\mathbf{y}} \quad (29)$$

where $\Phi_{\text{iron}} = [\varphi_{sy1}, \dots, \varphi_{syQ_s}, \varphi_{st1}, \dots, \varphi_{stQ_s}, \varphi_{ry1}, \dots, \varphi_{ryp}]^T$ and $\Phi_{\mathbf{y}} = [\varphi_{sy1}, \dots, \varphi_{syQ_s}, \varphi_{ry1}, \dots, \varphi_{ryp}]^T$. \mathbf{A}_{iron} is the incidence matrix. Then, the matrix form \mathbf{B}_{iron} of the iron flux density B_{iron} is calculated as

$$\mathbf{B}_{\text{iron}} = \mathbf{A}_{\text{iron}} \Phi_{\mathbf{y}} \mathbf{S}_{\text{iron}}^{-1} \quad (30)$$

where \mathbf{S}_{iron} is the matrix form of the cross-sectional area in the magnetic resistance.

When all elements of \mathbf{B}_{iron} are smaller than the saturation point of the electrical steel B_{sat} , it is sufficient to neglect iron saturation when predicting the corresponding performance of

the motor. Besides, at the initial design stage, to reduce iron losses and avoid iron nonlinearity, the flux density in the iron is kept near the saturation level of the electrical steel. Hence, the stator yoke height h_{sy} , the tooth width w_t , and the rotor yoke height h_{ry} are determined using

$$h_{sy} = \frac{\varphi_{sy_max}}{B_{sat}l_{eff}}, w_t = \frac{\varphi_{st_max}}{B_{sat}l_{eff}}, h_{ry} = \frac{\varphi_{ry_max}}{B_{sat}l_{eff}} \quad (31)$$

where φ_{sy_max} , φ_{st_max} , and φ_{ry_max} are the maximum flux in the stator yoke, stator tooth, and rotor yoke for one electric period.

D. Iron Saturation

When the elements of \mathbf{B}_{iron} are smaller than B_{sat} , the corresponding resistances in the magnetic circuit keep unchanged using (28). For the elements of \mathbf{B}_{iron} that are larger than B_{sat} , the simplified relationship between iron flux density B and the magnetic field strength H is given as

$$B = k_{sat2}H + B_{sat2} \quad (32)$$

where k_{sat2} and B_{sat2} are the slope and the intercept of the simplified BH curve in the saturated region of Fig. 5. The magnetic potential drop in each magnetic circuit U_{iron} is expressed as

$$U_{iron} = H_{iron}l_{iron} = \frac{l_{iron}}{k_{sat}S_{iron}}\varphi_{iron} - \frac{B_{sat0}}{k_{sat}}l_{iron} \quad (33)$$

where S_{iron} is the element of the matrix \mathbf{S}_{iron} . l_{iron} is the length of the magnetic resistance. $k_{sat} = k_{sat1}$ and $B_{sat0} = 0$ for $B_{iron} < B_{sat}$ while $k_{sat} = k_{sat2}$ and $B_{sat0} = B_{sat2}$ for $B_{iron} \geq B_{sat}$, which is defined in Fig. 5. Accordingly, (28) is manipulated as

$$\begin{aligned} \frac{\varphi_{sy1}}{k_{sat}} + \frac{\varphi_{sy2}}{k_{sat}} + \dots + \frac{\varphi_{syQ_s}}{k_{sat}} &= \sum \frac{B_{sat0}S_{sy}}{k_{sat}} \\ \frac{\varphi_{ry1}}{k_{sat}} + \frac{\varphi_{ry2}}{k_{sat}} + \dots + \frac{\varphi_{ryp}}{k_{sat}} &= \sum \frac{B_{sat0}S_{ry}}{k_{sat}}. \end{aligned} \quad (34)$$

The iron saturation can be represented using the equivalent saturation current \mathbf{I}_{sat} , which has proved effective in [15]

$$\mathbf{I}_{sat} = \mathbf{C}_r \mathbf{U}_{iron} \quad (35)$$

where \mathbf{U}_{iron} is the matrix of U_{iron} and \mathbf{C}_r is the constant matrix that represents the linear relationship between \mathbf{I}_{sat} and \mathbf{U}_{iron} . \mathbf{I}_{sat} is placed at the same position as the winding current to reduce the computational burden, as the same expression between the flux and the winding current can be used to show the influence of iron saturation. But unlike the iterative method in [15] for obtaining the equivalent saturation current, it is directly calculated based on the simplified BH curve in Fig. 5. Then, \mathbf{I}_{sat} is expressed as

$$\begin{aligned} \mathbf{I}_{sat} &= \mathbf{C}_r \mathbf{U}_{iron} = \mathbf{C}_r \mathbf{R}_{iron} \Phi_{iron} - \mathbf{C}_r \mathbf{U}_{sat0} \\ &= \mathbf{C}_r \mathbf{R}_{iron} \mathbf{A}_{iron} \Phi_y - \mathbf{C}_r \mathbf{U}_{sat0} \end{aligned} \quad (36)$$

where \mathbf{R}_{iron} and \mathbf{U}_{sat0} are the matrices of the slope and y-intercept from (33), which represents the iron saturation in the analytical model. They are determined after \mathbf{B}_{iron} is calculated using (30). Then, the flux flowing into the stator and rotor iron is

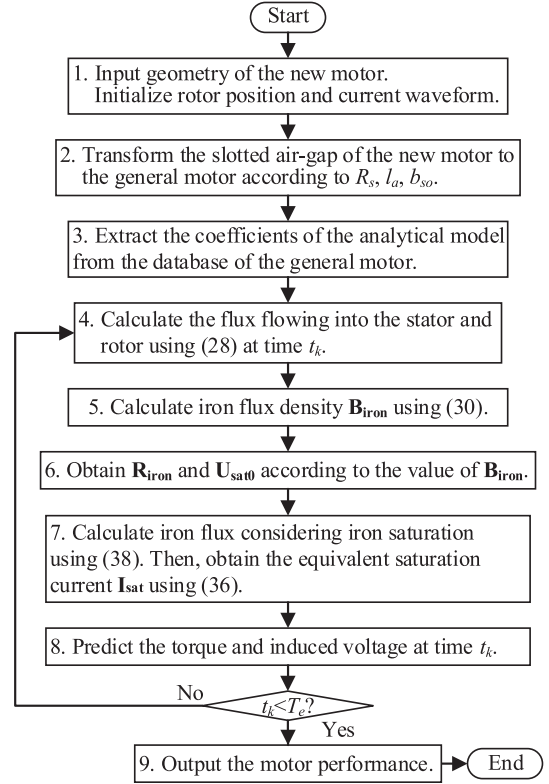


Fig. 6. Flowchart of SAM.

updated by including the extra flux produced by the equivalent saturation current

$$\begin{aligned} \mathbf{A}_{ty} \Phi_y &= \Phi_{PM} + \Phi_w + \Phi_{sat} \\ &= \Phi_{PM} + \mathbf{K}_t \mathbf{I}_w + \mathbf{K}_t \mathbf{I}_{sat} \\ &= \Phi_{PM} + \mathbf{K}_t \mathbf{I}_w + \mathbf{K}_t \mathbf{C}_r \mathbf{R}_{iron} \mathbf{A}_{iron} \Phi_y - \mathbf{K}_t \mathbf{C}_r \mathbf{U}_{sat0} \end{aligned} \quad (37)$$

where \mathbf{A}_{ty} is defined in (26) and (27). Φ_{PM} and \mathbf{K}_t are the matrix form of the flux generated by PMs and unit winding current flowing into the stator tooth and rotor yoke, respectively. They are derived from (14) using the superposition principle. Then, according to (37), the flux in stator yoke and rotor yoke Φ_y is calculated using

$$\begin{aligned} \Phi_y &= (\mathbf{A}_{ty} - \mathbf{K}_t \mathbf{C}_r \mathbf{R}_{iron} \mathbf{A}_{iron})^{-1} (\Phi_{PM} + \mathbf{K}_t \mathbf{I}_w \\ &\quad - \mathbf{K}_t \mathbf{C}_r \mathbf{U}_{sat0}). \end{aligned} \quad (38)$$

Accordingly, the air-gap flux density, flux linkage, back-EMF, and torque can be updated by including the magnetic field produced from \mathbf{I}_{sat} using (36). Fig. 6 gives the flowchart to predict the motor performance using SAM considering iron saturation.

III. SCALABLE SPM MOTORS

One small and one large SPM motor are analyzed to verify the effectiveness of the SAM. Their outer diameters are 120 mm and 10 m, respectively. Other motor parameters are given in

TABLE I
PARAMETERS OF THE SMALL AND LARGE SPM MOTOR

Parameter	Small Motor	Large Motor	Unit
Pole number	4	280	/
Slot number	36	240	/
Air-gap outer diameter	74	9700	mm
Airgap inner diameter	70.8	9680	mm
Magnet thickness	2.5	50	mm
Pole-arc to pole-pitch ratio	0.8	0.93	/
Motor inner diameter	30	9274	mm
Slot opening	2.5	50.2	mm
Stator yoke height	10.0	36.9	mm
Effective length	70	2000	mm
Tooth width	3.4	50.5	mm
Turns of coil	13	14	/
Rotational speed	3000	7	rpm
Load current (RMS)	20	2000	A

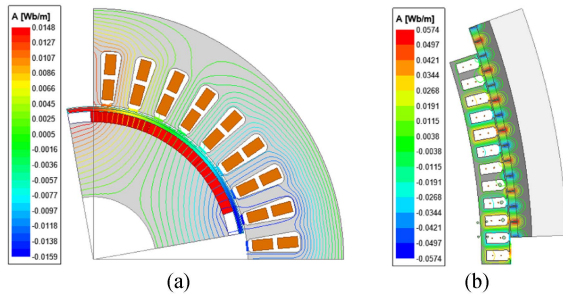


Fig. 7. Flux distribution of the small and large SPM motor. (a) Small SPM motor. (b) Large SPM motor.



Fig. 8. Stator and rotor of the small SPM prototype.

Table I. The finite-element analysis is carried out using Ansys Electronics 2022 to verify the proposed model in Fig. 7. The prototype of the 4-pole and 36-slot SPM motor is built and tested to show the accuracy of the SAM, as shown in Fig. 8.

The SAM can accurately predict the air-gap flux density for both small and large SPM motors, as shown in Figs. 9 and 10. Then, the flux linkage and back-EMF are predicted using (15) and (38). Figs. 11 and 12 give the comparison of flux linkage predicted using the SAM and FEM for both motors. When neglecting the slotting effect in the SAM, the prediction errors of flux linkage increase from 3.6% to 7.8% and from 3.8% to 7.7% for small and large motors, respectively. The experimental back-EMF is measured and compared with the SAM and FEM for the small SPM motor in Fig. 13. The error of back-EMF

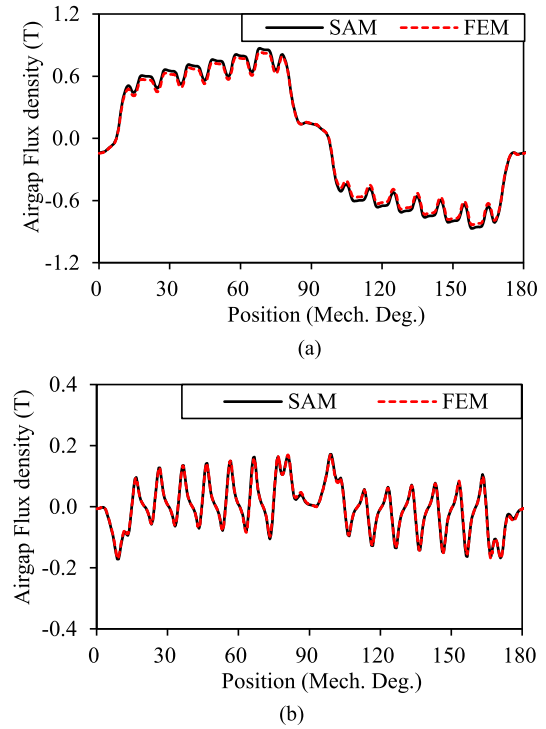


Fig. 9. On-load air-gap flux density for the small motor. (a) Radial. (b) Tangential.

prediction using SAM neglecting the slotting effect increases from 0.6% to 3.2%. For the back-EMF of the large motor, the waveform is shown in Fig. 14, and the prediction error of the SAM is 3.6% and 6.3% when considering and neglecting the slotting effect, respectively. It can be seen that the slotting effect will significantly affect the prediction accuracy of flux linkage and back-EMF. Hence, it is necessary to consider the slotting effect in the SAM. The self and mutual inductances of the small motor using SAM are $386 \mu\text{H}$ and $150 \mu\text{H}$, respectively. Accordingly, their FEM calculations are 407 and $154 \mu\text{H}$. As for the large motor, the self and mutual inductances using either SAM or FEM are 613 , 68.8 , 605 , and $55.1 \mu\text{H}$, respectively.

Then, the flux linkage through one tooth and one yoke for both motors at rated current is obtained using (26)–(28) and the SAM calculations are compared with FEM results in Figs. 15 and 16. The stator tooth and yoke flux predicted using SAM agrees well with FEM results considering iron saturation. As the saturation points of electrical steel for both motors are 1.5 T , the initial design for stator yoke height and the tooth width can be obtained using (31). For the small motor, $h_{sy} = 10.8 \text{ mm}$ and $w_t = 3.5 \text{ mm}$. For the large motor, $h_{sy} = 25.0 \text{ mm}$ and $w_t = 47.2 \text{ mm}$. Then, the optimization algorithm using FEM is employed to obtain the final design of both motors. Compared with the parameter of the final design in Table I, they are very close for both SPM motors except for the stator yoke height of the large motor. This is because the mechanical constraints are not considered in the initial design using (31). Nevertheless, SAM can accurately predict the motor performance in the final design due to considering both saturation effect and slotting effect, as given below.

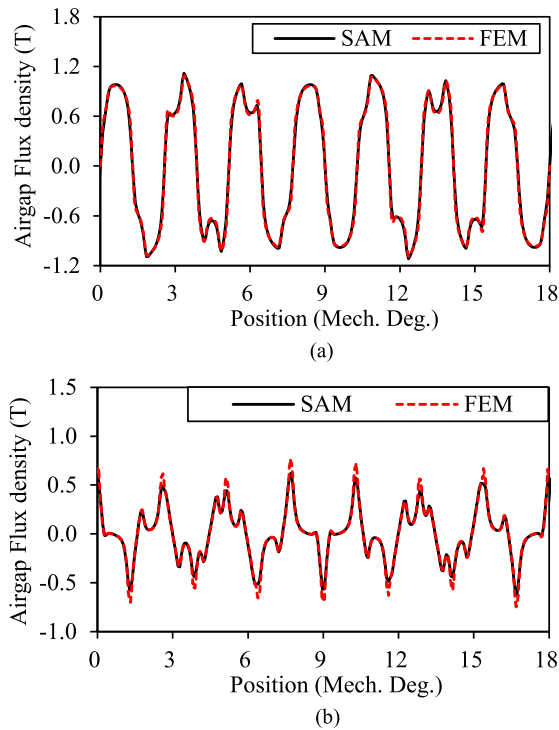


Fig. 10. On-load air-gap flux density for the large motor. (a) Radial. (b) Tangential.

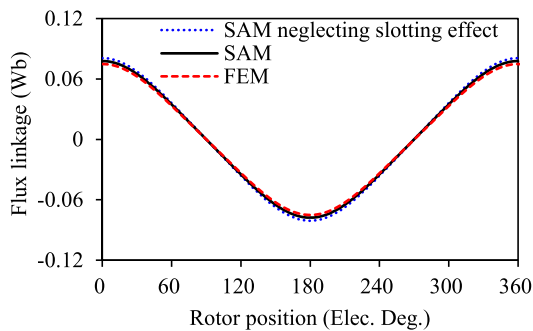


Fig. 11. Open-circuit flux linkage for the small motor.

The SAM can accurately calculate the performance of the torque and electromagnetic force, as shown in Figs. 17–20. The torque predictions using SAM agree well with FEM calculations and experimental results, even when the input current is high, due to the included iron saturation. In Figs. 19 and 20, the largest errors of the average force using SAM for both motors are 6.2% and 7.0%, respectively. The force ripple can be accurately predicted for the 4-pole/36-slot motors in Fig. 19. They demonstrate great accuracy of electromagnetic force prediction using SAM.

The comparisons of the PM loss and iron loss for both motors are given in Figs. 21 and 22. The SAM predictions agree well with FEM results. As for the copper loss, (23) and (24) are used for both motors using FEM and SAM. Therefore, the FEM and SAM prediction of copper loss are the same. The efficiency of both motors is shown in Figs. 23 and 24, where SAM still exhibits great accuracy at different input currents.

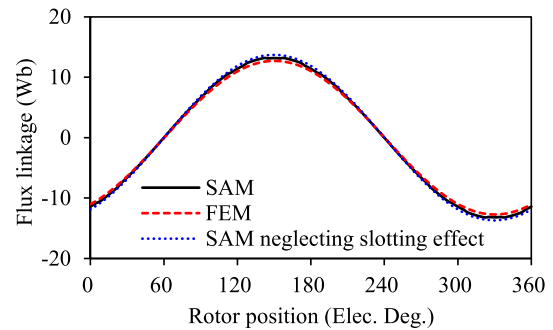


Fig. 12. Open-circuit flux linkage for the large motor.

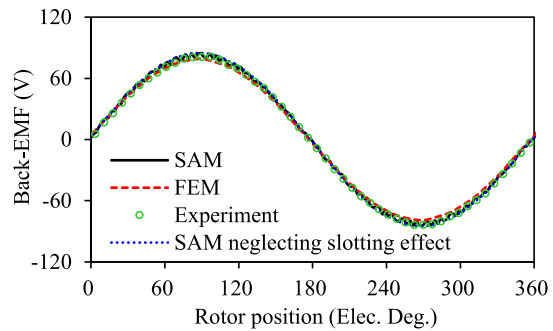


Fig. 13. Open-circuit back-EMF for the small motor.

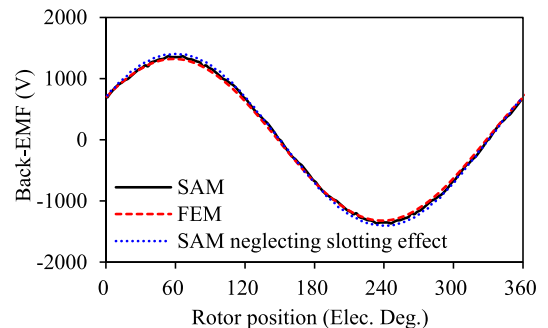


Fig. 14. Open-circuit back-EMF for the large motor.

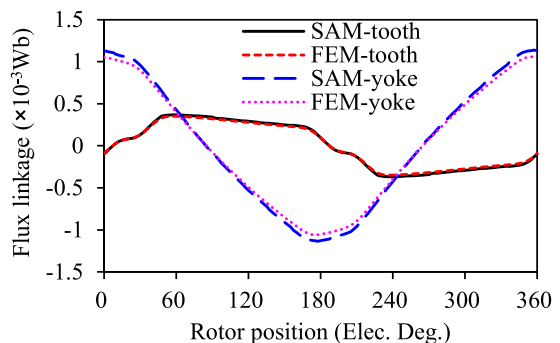


Fig. 15. Tooth and yoke flux linkage for the small SPM motor at rated current.

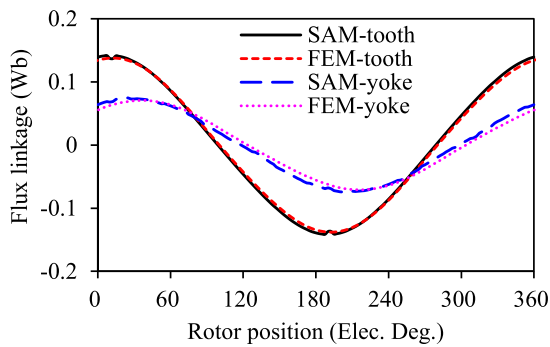


Fig. 16. Line flux linkage for the large SPM motor at rated current.

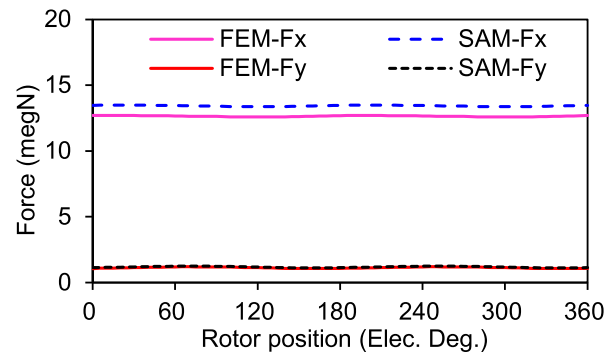


Fig. 20. Force waveform of the large SPM motor at 2000 A.

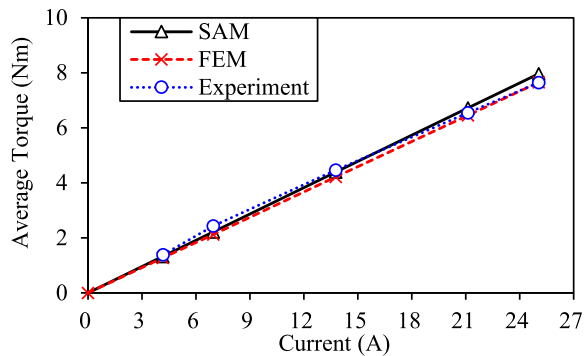


Fig. 17. Average torque of the small SPM motor at different currents.

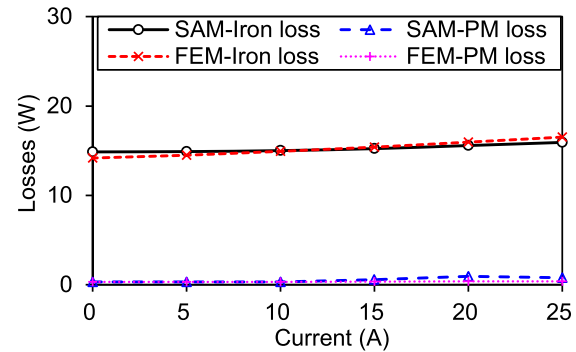


Fig. 21. PM loss and iron loss of the small SPM motor at different currents.

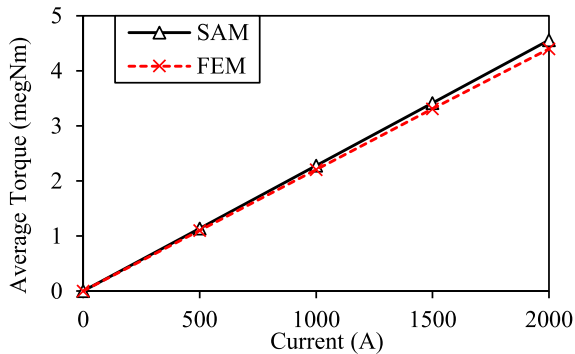


Fig. 18. Average torque of the large SPM motor at different currents.

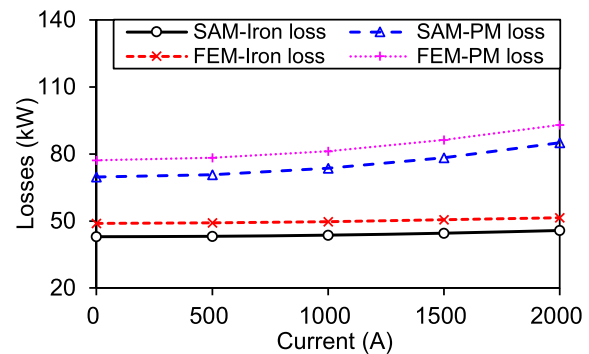


Fig. 22. PM loss and iron loss of the large SPM motor at different currents.

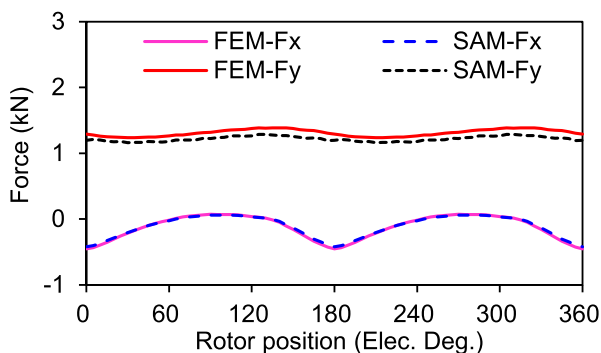


Fig. 19. Force waveform of the small SPM motor at 20 A.

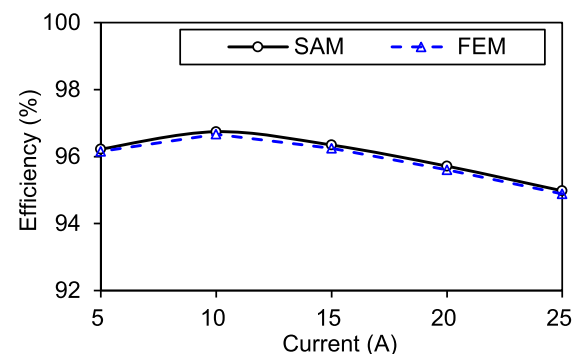


Fig. 23. Efficiency of the small SPM motor at different currents.

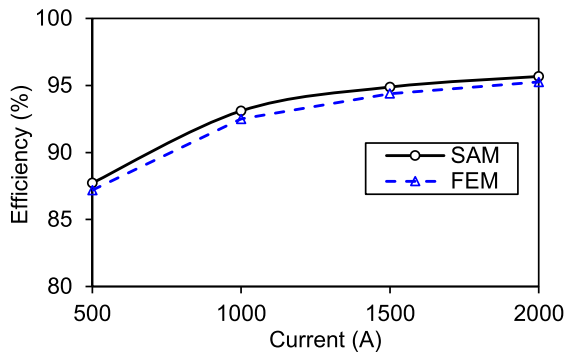


Fig. 24. Efficiency of the large SPM motor at different currents.

TABLE II

COMPARISON AMONG DIFFERENT ANALYTICAL MODELS FOR THE SMALL SPM MOTOR

		SAM	ECM [24]	HAM [29]	FEM	Test
Back-EMF	Value (V)	82.8	81.8	82.0	78.6	82.1
	Error	0.8%	0.4%	0.1%	4.2%	/
Rated Torque	Value (Nm)	6.72	6.74	6.70	6.46	6.55
	Error	2.6%	2.9%	2.3%	1.4%	/
Solving Time (s)		64.1	139	298	1376	/

TABLE III

COMPARISON AMONG DIFFERENT ANALYTICAL MODELS FOR THE LARGE SPM MOTOR

		SAM	ECM [24]	HAM [29]	FEM
Back-EMF	Value (V)	1363	1410	1352	1320
	Error	3.3%	6.8%	2.4%	/
Rated Torque	Value (megNm)	4.56	4.72	4.49	4.40
	Error	3.6%	7.2%	2.0%	/
Calculation Time		38	101	98	2037

The proposed model is also compared with exact conformal mapping (ECM) in [24] and hybrid analytical model (HAM) in [29] to show the advantage of the SAM in Tables II and III. The ECM conformally transforms the whole air-gap region into the annular region while neglecting saturation. Hence, it is time-consuming with worse accuracy compared to SAM for rated torque prediction of both motors. As for HAM, only one-slot air-gap region is used to consider slotting effect, and it requires iterative calculation to determine the saturation level. Therefore, it takes longer time for HAM to calculate the motor performance than SAM, while their prediction accuracy is comparable, whose errors are less than 3.6%. Moreover, the SAM builds the internal connection among different SPM motors regardless of the motor power and dimension, while ECM and HAM cannot evolve from the previous calculation of SPM motor.

IV. CONCLUSION

In this article, the SAM is developed to calculate the magnetic field of the SPM motors based on the conformal mapping technique. It requires only one general motor and establishes the corresponding database of SC mapping. Then, the relationship between the new SPM motor and the general motor is expressed using the explicit formula of conformal mapping, making the

analytical model more direct to reveal the relationship between the motor performance and the motor geometry. The SAM was suitable for any SPM motor with either an outer rotor or an inner rotor and different slot/pole combinations. The small-scale SPM motor with an outer diameter of 120 mm and the large-scale motor with an outer diameter of 10 m were designed to validate the effectiveness of the proposed model and the scaling law of the SPM motors. Moreover, the data from the optimized motor or prototype can be theoretically used to obtain or validate new designs based on the proposed SAM regardless of the motor power and geometry, which is one of our future works.

REFERENCES

- [1] Z. Yang, F. Shang, I. P. Brown, and M. Krishnamurthy, "Comparative study of interior permanent magnet, induction, and switched reluctance motor drives for EV and HEV applications," *IEEE Trans. Transp. Electric.*, vol. 1, no. 3, pp. 245–254, Oct. 2015.
- [2] G. Pellegrino, A. Vagati, B. Boazzo, and P. Guglielmi, "Comparison of induction and pm synchronous motor drives for EV application including design examples," *IEEE Trans. Ind. Appl.*, vol. 48, no. 6, pp. 2322–2332, Nov./Dec. 2012.
- [3] W. Cao, B. C. Mecrow, G. J. Atkinson, J. W. Bennett, and D. J. Atkinson, "Overview of electric motor technologies used for more electric aircraft (MEA)," *IEEE Trans. Ind. Electron.*, vol. 59, no. 9, pp. 3523–3531, Sep. 2012.
- [4] T. Zhao, S. Wu, and S. Cui, "Multiphase PMSM with asymmetric windings for more electric aircraft," *IEEE Trans. Transp. Electric.*, vol. 6, no. 4, pp. 1592–1602, Dec. 2020.
- [5] M. Qiao, C. Jiang, Y. Zhu, and G. Li, "Research on design method and electromagnetic vibration of six-phase fractional-slot concentrated-winding pm motor suitable for ship propulsion," *IEEE Access*, vol. 4, pp. 8535–8543, 2016.
- [6] Y. Duan and D. M. Ionel, "A review of recent developments in electrical machine design optimization methods with a permanent-magnet synchronous motor benchmark study," *IEEE Trans. Ind. Appl.*, vol. 49, no. 3, pp. 1268–1275, May/Jun. 2013.
- [7] G. Y. Sizov, D. M. Ionel, and N. A. O. Demerdash, "Modeling and parametric design of permanent-magnet AC machines using computationally efficient finite-element analysis," *IEEE Trans. Ind. Electron.*, vol. 59, no. 6, pp. 2403–2413, Jun. 2012.
- [8] V. Rallabandi, J. Wu, P. Zhou, D. G. Dorrell, and D. M. Ionel, "Optimal design of a switched reluctance motor with magnetically disconnected rotor modules using a design of experiments differential evolution FEA-based method," *IEEE Trans. Magn.*, vol. 54, no. 11, Nov. 2018, Art. no. 8205705.
- [9] W. Zhao, A. Ma, J. Ji, X. Chen, and T. Yao, "Multi-objective optimization of a double-side linear Vernier PM motor using response surface method and differential evolution," *IEEE Trans. Ind. Electron.*, vol. 67, no. 1, pp. 80–90, Jan. 2020.
- [10] J. W. Bandler et al., "Space mapping: The state of the art," *IEEE Trans. Microw. Theory Techn.*, vol. 52, no. 1, pp. 337–361, Jan. 2004.
- [11] J. Gong, F. Gillon, J. T. Canh, and Y. Xu, "Proposal of a Kriging output space mapping technique for electromagnetic design optimization," *IEEE Trans. Magn.*, vol. 53, no. 6, Jun. 2017, Art. no. 8106004.
- [12] G. Crevecoeur, L. Dupre, and R. Van de Walle, "Space mapping optimization of the magnetic circuit of electrical machines including local material degradation," *IEEE Trans. Magn.*, vol. 43, no. 6, pp. 2609–2611, Jun. 2007.
- [13] S. Stipetic, J. Goss, D. Zarko, and M. Popescu, "Calculation of efficiency maps using a scalable saturated model of synchronous permanent magnet machines," *IEEE Trans. Ind. Appl.*, vol. 54, no. 5, pp. 4257–4267, Sep./Oct. 2018.
- [14] S. Stipetic, D. Zarko, and M. Popescu, "Ultra-fast axial and radial scaling of synchronous permanent magnet machines," *Inst. Eng. Technol. Elect. Power Appl.*, vol. 10, pp. 658–666, 2016.
- [15] Z. Li et al., "An improved hybrid field model for calculating on-load performance of interior permanent-magnet motors," *IEEE Trans. Ind. Electron.*, vol. 68, no. 10, pp. 9207–9217, Oct. 2021.
- [16] L. J. Wu, Z. Q. Zhu, D. Staton, M. Popescu, and D. Hawkins, "Subdomain model for predicting armature reaction field of surface-mounted permanent-magnet machines accounting for tooth-tips," *IEEE Trans. Magn.*, vol. 47, no. 4, pp. 812–822, Apr. 2011.

- [17] L. J. Wu, Z. Q. Zhu, D. Staton, M. Popescu, and D. Hawkins, "Analytical model of eddy current loss in windings of permanent-magnet machines accounting for load," *IEEE Trans. Magn.*, vol. 48, no. 7, pp. 2138–2151, Jul. 2012.
- [18] W. Tong, L. Sun, S. Wu, M. Hou, and R. Tang, "Analytical model and experimental verification of permanent magnet eddy current loss in permanent magnet machines with nonconcentric magnetic poles," *IEEE Trans. Ind. Electron.*, vol. 69, no. 9, pp. 8815–8824, Sep. 2022.
- [19] Z. Li, X. Huang, Z. Chen, L. Wu, Y. Shen, and T. Shi, "Electromagnetic analysis for interior permanent-magnet machine using hybrid subdomain model," *IEEE Trans. Energy Convers.*, vol. 37, no. 2, pp. 1223–1232, Jun. 2022.
- [20] Y. Oner, Z. Q. Zhu, L. J. Wu, X. Ge, H. Zhan, and J. T. Chen, "Analytical on-load subdomain field model of permanent-magnet vernier machines," *IEEE Trans. Ind. Electron.*, vol. 63, no. 7, pp. 4105–4117, Jul. 2016.
- [21] P. Liang, F. Chai, Y. Li, and Y. Pei, "Analytical prediction of magnetic field distribution in spoke-type permanent-magnet synchronous machines accounting for bridge saturation and magnet shape," *IEEE Trans. Ind. Electron.*, vol. 64, no. 5, pp. 3479–3488, May 2017.
- [22] Z. Q. Zhu and D. Howe, "Instantaneous magnetic field distribution in brushless permanent magnet DC motors. III. Effect of stator slotting," *IEEE Trans. Magn.*, vol. 29, no. 1, pp. 143–151, Jan. 1993.
- [23] D. Žarko, D. Ban, and T. A. Lipo, "Analytical calculation of magnetic field distribution in the slotted air gap of a surface permanent-magnet motor using complex relative air-gap permeance," *IEEE Trans. Magn.*, vol. 42, no. 7, pp. 1828–1837, Jul. 2006.
- [24] T. C. O'Connell and P. T. Krein, "A Schwarz-Christoffel-based analytical method for electric machine field analysis," *IEEE Trans. Energy Convers.*, vol. 24, no. 3, pp. 565–577, Sep. 2009.
- [25] H.-K. Yeo, D.-K. Lim, D.-K. Woo, J.-S. Ro, and H.-K. Jung, "Magnetic equivalent circuit model considering overhang structure of a surface-mounted permanent-magnet motor," *IEEE Trans. Magn.*, vol. 51, no. 3, Mar. 2015, Art. no. 8201004.
- [26] X. Huang, M. Zhu, W. Chen, J. Zhang, and Y. Fang, "Dynamic reluctance mesh modeling and losses evaluation of permanent magnet traction motor," *IEEE Trans. Magn.*, vol. 53, no. 6, Jun. 2017, Art. no. 8102804.
- [27] D. Cao, W. Zhao, J. Ji, and Y. Wang, "Parametric equivalent magnetic network modeling approach for multi-objective optimization of PM machine," *IEEE Trans. Ind. Electron.*, vol. 68, no. 8, pp. 6619–6629, Aug. 2021.
- [28] L. Wu, H. Yin, D. Wang, and Y. Fang, "On-load field prediction in SPM machines by a subdomain and magnetic circuit hybrid model," *IEEE Trans. Ind. Electron.*, vol. 67, no. 9, pp. 7190–7201, Sep. 2020.
- [29] Z. Li, X. Huang, J. Ma, Z. Chen, A. Liu, and L. Peretti, "Hybrid analytical model for predicting the electromagnetic losses in surface-mounted permanent-magnet motors," *IEEE Trans. Transp. Electrification*, to be published, doi: [10.1109/TTE.2023.3289869](https://doi.org/10.1109/TTE.2023.3289869).
- [30] A. Hanic, D. Zarko, D. Kuhinek, and Z. Hanic, "On-load analysis of saturated surface permanent magnet machines using conformal mapping and magnetic equivalent circuits," *IEEE Trans. Energy Convers.*, vol. 33, no. 3, pp. 915–924, Sep. 2018.
- [31] T. A. Driscoll and S. A. Vavasis, "Numerical conformal mapping using cross-ratios and delaunay triangulation," *SIAM J. Sci. Comput.*, vol. 19, no. 6, pp. 1783–1803, Jan. 1998.
- [32] X. Li, X. Wang, and Z. Xing, "Analysis and research on local irreversible demagnetization of inverter-powered PM motor," *IEEE Trans. Ind. Electron.*, vol. 71, no. 6, pp. 5618–5629, Jun. 2024.
- [33] B. Guo, Y. Huang, F. Peng, and J. Dong, "General analytical modeling for magnet demagnetization in surface mounted permanent magnet machines," *IEEE Trans. Ind. Electron.*, vol. 66, no. 8, pp. 5830–5838, Aug. 2019.
- [34] Z. Li, X. Huang, A. Liu, Z. Chen, Y. Yu, and L. Wu, "Analytical calculation of eccentric surface-mounted permanent-magnet motor accounting for iron saturation," *IEEE Trans. Transp. Electrification*, vol. 8, no. 3, pp. 3441–3450, Sep. 2022.
- [35] D. Lin, P. Zhou, W. N. Fu, Z. Badics, and Z. J. Cendes, "A dynamic core loss model for soft ferromagnetic and power ferrite materials in transient finite element analysis," *IEEE Trans. Magn.*, vol. 40, no. 2, pp. 1318–1321, Mar. 2004.
- [36] G. Liu, M. Liu, Y. Zhang, H. Wang, and C. Gerada, "High-speed permanent magnet synchronous motor iron loss calculation method considering multiphysics factors," *IEEE Trans. Ind. Electron.*, vol. 67, no. 7, pp. 5360–5368, Jul. 2020.
- [37] J. Barta, N. Uzhegov, L. Knebl, and C. Ondrusek, "Effect of additional copper losses on the high-speed induction machine performance," in *Proc. 8th Int. Conf. Elect. Mach.*, 2018, pp. 1163–1168.



Zhaokai Li (Member, IEEE) received the B.S. and Ph.D. degrees from Zhejiang University, Hangzhou, China, in 2015 and 2020, respectively, both in electrical engineering.

He was a visiting student at the University of Cambridge from 2018 to 2019. He worked at Zhejiang University as a Postdoctoral Researcher from 2020 to 2022 and then continued his Postdoctoral Research with KTH Royal Institute of Technology, Sweden. Since September 2023, he has been a Guest Researcher with

ABB Corporate Research in Västerås Sweden. His research interests include analytical models and iron loss analysis for permanent magnet motors.



Xiaoyan Huang (Member, IEEE) received the B.E. degree in control measurement techniques and instrumentation from Zhejiang University, Hangzhou, China, in 2003, and the Ph.D. degree in electrical machines and drives from the University of Nottingham, Nottingham, U.K., in 2008.

From 2008 to 2009, she was a Research Fellow with the University of Nottingham. She is currently a Professor with the College of Electrical Engineering, Zhejiang University. Her research interests include PM machines and drives for aerospace and traction applications, and generator system for urban networks.



Luca Peretti (Senior Member, IEEE) was born in 1980. He received the M.Sc. degree in industrial engineering from the University of Udine, Udine, Italy, in 2005, and the Ph.D. degree in industrial engineering from the University of Padova, Padova, Italy, in 2009.

He worked at ABB Corporate Research, Sweden, between 2010 and 2018 before joining KTH Royal Institute of Technology, Sweden, as an Associate Professor. His research interests include (multiphase) machines and drives, their

control, and diagnostics, for industrial, renewable, and automotive applications.